POLITECNICO DI TORINO
Repository ISTITUZIONALE

Revisiting the identity of -MgCl2: Part II. Morphology and exposed surfaces studied by vibrational spectroscopies and DFT calculation

(Article begins on next page)

26 December 2024

Revisiting the identity of δ-MgCl₂: Part II. Morphology and exposed surfaces studied by vibrational spectroscopies and DFT calculation.

Alessandro Piovano,*[,‡,§] Maddalena D'Amore,*[,‡] Toru Wada,[†,§] Paolo Cleto Bruzzese,[‡] Gentoku Takasao,[†] Ashutosh Thakur,[†] Patchanee Chammingkwan,[†,§] Minoru Terano[†,§], Bartolomeo Civalleri,[‡] Silvia Bordiga,[‡] Toshiaki Taniike,[†,§] and Elena Groppo[‡,§]

[‡] Department of Chemistry, INSTM and NIS Centre, University of Torino, Via Giuria 7, 10125 Torino, Italy

[§] Dutch Polymer Institute, P.O. Box 902, 5600 AX Eindhoven, the Netherlands

[†] Graduate School of Advanced Science and Technology, Japan Advanced Institute of Science and Technology, 1-1 Asahidai, Nomi, Ishikawa, 923-1292, Japan

ABSTRACT

The activation of $MgCl_2$ is an essential step for preparing performant Ziegler-Natta (ZN) catalysts for olefin polymerization, either by mechanical grinding of pristine $MgCl_2$ or by chemical conversion of a precursor. Depending on the adopted activation process, different nanostructures are obtained in terms of disorder and morphology, which in turn influence the overall catalytic performance. In this work, we focused on the morphology of δ-$MgCl_2$ nanoparticles (i.e. the relative extension of the exposed surfaces), by investigating with vibrational spectroscopies a series of mechanically and chemically activated $MgCl_2$ samples, and by building up a comprehensive set of model structures (both ordered and disordered) and relative surfaces in order to highlight nanosizing effects and achieve an accurate description of $MgCl_2$ particles at an atomistic level. We found that both mechanical and chemical activation promote the expression of $MgCl_2$ surfaces exposing strongly acidic Mg^{2+} sites, which are those mostly involved in the catalysis, together with an increase of inter-surfaces edges, which have been recently considered as the main responsible for the ZNC stereo-selectivity.

1. INTRODUCTION

As long as the nano-sizing and the structural disorder are becoming predominant aspects in new catalytic materials [1], the morphology of the particles and the relative extension of the exposed surfaces must be considered as key players in the whole catalytic processes [2]. This is surely the case of $MgCl_2$-supported Ziegler-Natta (ZN) catalysts for olefin polymerization. These catalysts are intrinsically complex multi-component systems, whose composition is the result of a long optimization process, mostly achieved in an empirical manner, either through a trial and error approach [3] or through the more modern high-throughput screening of all the possible parameters [4]. In their current version, the main components that are dispersed on the surface of the $MgCl_2$ support material are the $TiCl_x$ species (the active phase), the AlR_3 co-catalyst, and some organic Lewis bases (LB, e.g. aromatic mono- and di-esters), introduced as electron donors to enhance the stereo-specificity of the catalysts in propylene polymerization [5, 6]. The irreplaceability of $MgCl_2$ as a support material relies on the unique advantages that it offers in terms of abundance and distribution of stereo-specific highly active sites [7-12], together with the regulation of the morphology of the produced polymer [13-15]. However, despite its fundamental role in the whole catalytic process, $MgCl_2$ still occupies the center of the black-box in the overall understanding of these catalysts.

The structural and surface properties of $MgCl_2$ strongly depend on its pre-treatment, a sort of activation that allows moving from the two crystalline polymorphs of $MgCl_2$ (α and β phases) to a high-surface-area material actually suitable for catalytic applications (δ-$MgCl_2$) [5]. Such a pre-treatment can vary from a mechanical grinding of the crystalline forms of $MgCl_2$ (in the absence or in presence of the other ingredients) [16-21] to the *in situ* conversion of a precursor (such as $MgCl_2$ in alcohol solution [22-25], adducts between $MgCl_2$ and Lewis bases [26-33], $Mg(OR)_2$ [25, 34-37], MgRX [38], and so on) into $MgCl_2$ in the course of the catalyst synthesis. The activation process is remarkably relevant because it influences the structure and the morphology of the $MgCl_2$ primary particles, which are then retained during the successive synthetic steps of the catalyst formation. Hence, the activation process of $MgCl_2$ ultimately drives the distribution of the active sites and their stereo-specificity [39-41], with direct and fundamental repercussions on the properties of the produced polymer.

Experimentally, the investigation of the activated δ-MgCl$_2$ is particularly challenging, because of its intrinsic structural disorder and nano-size, which is accompanied by an extreme air-sensitivity. This explains why so far most of the insights have been indirectly deduced from the analysis of the produced polymer [14, 42-45] since the introduction of δ-MgCl$_2$ in ZN catalysis [3, 5, 6]. A brief summary of the main achievements in the field of the structural analysis of δ-MgCl$_2$, as well as their historical development, has been provided in the introduction of the Part 1 of this work [46]. Here, the most significant past advances in understanding the morphology of the δ-MgCl$_2$ particles are reviewed. The first noticeable results based on the direct investigation of MgCl$_2$-based ZN catalysts were obtained on *ad hoc* synthesized model systems, formerly MgCl$_2$ thin films obtained from chemical vapor deposition [47-53], and latterly MgCl$_2$ platelets grown from the spin-coating of a MgCl$_2$-ROH solution in the presence of some electron donors, and then treated with TiCl$_4$ [27, 28, 54, 55]. In recent years, some of the authors have sharpened the use of FT-IR spectroscopy of adsorbed carbon monoxide as a technique to get information on the MgCl$_2$ exposed surfaces and their relative extent [30, 56]. The method, which was attempted for the very first time by Zakharov and co-workers [57], was demonstrated to be particularly powerful, especially when the MgCl$_2$ surfaces are not fully occupied by the other components and/or by side residues of the synthesis.

In parallel with the experiments, a great contribution to the overall understanding of δ-MgCl$_2$ (and of MgCl$_2$-based ZN catalysts in general) was traditionally provided by computational approaches, because of the possibility of modelling the isolated contribution of single surfaces or catalytic sites [58]. However, neither the theoretical chemistry can be decisive by itself, since the results strongly rely on the employed molecular models and on the advances in quantum chemistry, in particular in the Density Functional Theory (DFT). To make short a long history, the seminal MgCl$_2$ models as obtained from molecular mechanics in the 1980s presented the (110) and (104) lateral surfaces as the putative surfaces for the adsorption of monomeric and stereo-selective dimeric TiCl$_x$ species, respectively [7, 59]. However, more recent DFT studies have claimed the crisis of those models, warning about the critical thermodynamic stability of TiCl$_x$ species on flat and regular MgCl$_2$ surfaces, and moving towards a much more complex morphology of the δ-MgCl$_2$ particles, where defective sites (such as steps, corners, and interfaces between two different surfaces) play a major role [60-68]. To be important, the necessity of finding a reasonable balance between

accuracy and computational feasibility has limited the study to small clusters or surfaces with a perfect periodicity.

In this work, we coupled experimental and theoretical techniques to describe the structural disorder and the morphology of nano-sized $MgCl_2$ particles in Ziegler-Natta catalysts. On one side, we systematically investigated an *ad hoc* prepared series of both mechanically and chemically activated $MgCl_2$ samples, exploiting in a concerted fashion several state-of-the-art characterization techniques to approach an atomic scale description of the structure and dynamics of δ-$MgCl_2$. This required the development of specific setups and protocols to operate under inert conditions [32, 69, 70]. On the other side, theoretical modelling was pushed a step forward with respect to previous computational works, through the construction of a comprehensive set of model structures with periodic boundary conditions at different dimensionality to describe events taking place at different scales [71], up to simulating the Wulff's plot of the whole $MgCl_2$ particles. Altogether, this study, coupled with the structural analysis carried out in the first part of this research [46], gives the most accurate and realistic description as possible of δ-$MgCl_2$ particles in ZN catalysts, providing the fundamental background for all those Companies who aspire to finely control the catalytic process of olefin polymerization.

2.EXPERIMENTAL METHODS

2.1 Samples

A ball-milled $MgCl_2$ was donated by Toho Titanium Co., Ltd. ($MgCl_2$ A, specific surface area: 9.3 $m^2 g^{-1}$). In order to enhance the specific surface area, 25 g of $MgCl_2$ A was filled in a 0.5 L stainless-steel pot with 235 stainless-steel balls (10 mm diameter) and subjected to planetary ball milling. Two milling times were adjusted to make the specific surface area about five and eight times higher than that of $MgCl_2$ A, respectively, and thus the obtained samples were termed as $MgCl_2$ B (specific surface area: 55 $m^2 g^{-1}$) and $MgCl_2$ C (specific surface area: 73 $m^2 g^{-1}$). A $Mg(OEt)_2$-based ZN pre-catalyst (hereafter labeled as ZNC) was prepared according to a patent [72] with slight modifications [35, 36, 39], where n-dibuthylphthalate (hereafter DBP) was used as an internal donor. The donor and Ti contents were determined as 14.1 wt% and 2.6 wt%, respectively. All the samples were stored and transferred thoroughly under an inert atmosphere in order to minimize the moisture adsorption.

2.2 FT-IR spectroscopy

FT-IR spectra were collected with a Bruker Vertex70 instrument, which was equipped with either a MCT detector for collecting the spectra in the Mid-IR region or a DTGS detector for collecting the spectra in the Far-IR region.

2.2.1 Far-IR measurements

Collection of transmission Far-IR spectra implied the realization and optimization of an ad-hoc experimental setup, overcoming some limitations intrinsic to the technique. In view of the novelty of the setup, a short description of the solutions adopted to overcome each limitation follows.

1) The low number of photons in comparison to Mid-IR implied a much lower signal-to-noise ratio, and an increased sensitivity towards any source of noise (e.g. water vapor, vibrations, and so on). To face this problem the Far-IR spectra were acquired at a resolution of 4 cm^{-1}, at the lowest possible scan rate of 2.5 kHz, and by accumulating 64 scans (for a total of 2 minutes per spectrum). Care was taken to collect the spectra with a perfectly clean instrumental chamber, so to compensate the signal of water vapor.

2) The very large beam size (ø of ca. 1.5 cm, even in the instrument focus) forced us to work with a large sample very homogeneous in thickness and composition. We could not work with thin pellets, as usually done in the Mid-IR region, since it was not possible to realize large pellets, at the same time sufficiently thin to allow an acceptable transmission, homogeneous and self-standing. We overcame the problem by depositing thin layers of each sample on a silicon wafer. Silicon is almost transparent in the Far-IR region and gives only a weak scattering profile, provided that it has a suitable purity and thickness to avoid the formation of interference fringes. The depositions were performed inside the glove-box, using hexane as a suspending agent.

3) The absence of commercial cells allowing to perform measurements in controlled atmosphere prompted us to build up our own experimental set-up. We adopted a quartz cell equipped with two polyethylene windows. Similar to silicon, polyethylene has almost no absorption in the Far-IR region, but only a partial scattering that further decreases the number of photons reaching the detector. After drying, the silicon wafer with the sample deposition was inserted in the cell, and brought

outside the glove-box. The measurements were all performed by maintaining the N_2 atmosphere, but the cell allows in principle to work in vacuum or in the presence of other gases. It is worth noticing that such an experimental set-up allowed us to collect the Far-IR spectrum of ZNC activated by TEAl, which has been never reported in the past.

All the acquired spectra are shown in absorbance, after subtraction of the weak contribution of the silicon wafer and of the polyethylene windows.

2.2.2 Mid-IR measurements

Measurements in the Mid-IR region were performed on samples in the form of thin self-supporting pellets (surface density of ca. 50 mg/cm^2). The pellet was prepared directly inside the glove-box to avoid contamination. After evaluation of the surface area and of the weight (necessary to calculate the optical density), the pellet was introduced in a gold envelope to confer mechanical resistance, and then inserted within a quartz cell equipped with two KBr windows. The cell allows performing measurements in vacuum and/or in the presence of a controlled amount of gases, in a temperature range from 100 to 300 K.

The FT-IR spectra of CO adsorption at 100 K were performed according to the following protocol. A first spectrum of the sample was collected at room temperature under vacuum. Then, CO was dosed at room temperature and at an equilibrium pressure of $P_{CO} =$ 50 mbar, and the temperature was decreased down to 100 K. FT-IR spectra were collected at 100 K at the maximum CO coverage (θ_{max}), and upon gradually decreasing θ through controlled expansions, up to the complete desorption. All the spectra are shown after subtraction of the spectrum of the sample measured prior to the CO addition, and after normalization to the optical thickness of the pellets.

3. MODELS AND COMPUTATIONAL DETAILS

3.1 Models of disordered and nanostructured MgCl$_2$

3.1.1 Ordered and disordered MgCl$_2$ models

The ordered α and β forms of MgCl$_2$ are layered structures differing in the stacking of the planes of chlorine atoms along the c-axis, which is of the (…ABCABC…) cubic type for the α phase, and of the (…ABABAB…) hexagonal type for the β one. By starting from the optimized unit cell of α and β MgCl$_2$ polymorphs, periodic "supercells" were built with multiple periodicity along *c* axis. Three disordered δ models were then obtained creating mixed

phases from the α and β ones as shown in Figure 1. Models δ_1 and δ_2 were built to simulate a translational stacking fault disorder by inserting different portions of β layers in between α layers. Model δ_3 was obtained from the α form by a simple rotation of +60° around the c axis. Models δ_1 and δ_2 feature a triclinic P1 group symmetry, while model δ_3 preserves twelve symmetry operations as for the ordered α and β forms.
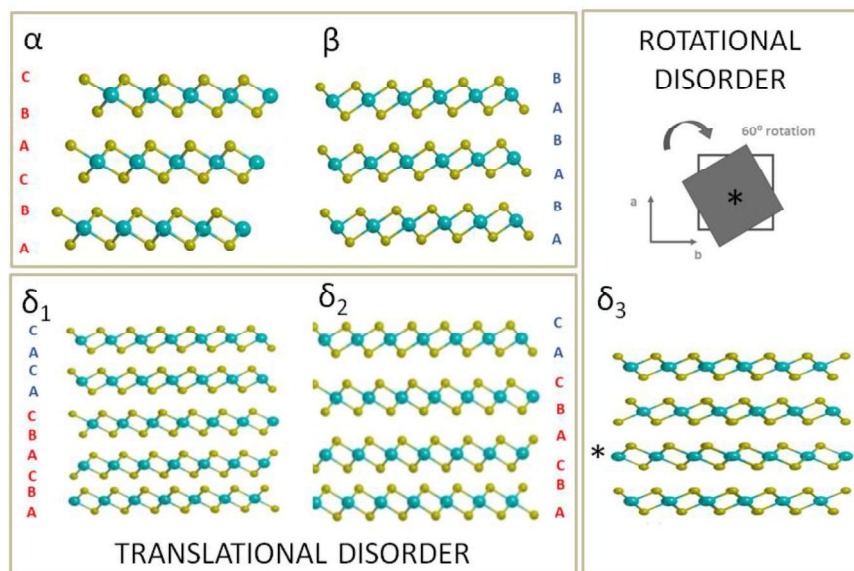

Figure 1. Lateral view of the Cl-Mg-Cl layers along the c axis in ordered α and β polymorphs of $MgCl_2$ and in disordered models δ_1 and δ_2 (which reproduce a translational disorder) and δ_3 (which reproduces a rotational disorder, as pointed out by the asterisk).

3.1.2 $MgCl_2$ surfaces and prediction of the crystal shape.

$MgCl_2$ surfaces were modelled by resorting to a slab approach, carefully checking that the surface formation energy converged upon increasing the slab thickness. In 2D-periodic slab models, when possible, at least the inversion or a mirror operator was kept. The thermodynamically most stable surfaces were determined according to the Bravais' law. At equilibrium, for a given temperature T, a small crystal has a specific shape that corresponds to a crystal with exposed hkl faces such that the integration of the energy over the entire surface area A is minimal, $\int_A \gamma(hkl)dA(hkl) = min$, i.e. in isobaric conditions the total surface Gibbs free energy according to the Wulff-Gibbs theorem is a minimum. As a first approximation, the internal energy is often adopted as state function for predicting the crystal shape and morphology and many "black box" computational tools generate finite crystals in this way. Here, we predicted the crystal morphology of $MgCl_2$ by referring to

surface formation energies (i.e. the energy spent to form the surface from the bulk per surface area) of selected faces (namely (001), (012), (104), (015), (107), and (110)) on the base of both internal energies (E_s) and Gibbs free energies (G_s).

3.2 Computational details

3.2.1 Theoretical methods and geometry optimization

Calculations were performed using B3LYP-D* functional that includes a dispersion semi-empirical DFT-D2 correction [73] as refitted for crystalline systems [74]. The PBE0-D3 method [75] including a three body correction for dispersion energy was also assessed. However, the results are very similar to those obtained by B3LYP-D*, and therefore not discussed hereafter.

All calculations were performed using the distributed parallel version of the periodic *ab initio* CRYSTAL17 code (MPPCRYSTAL) [76]. This version features an excellent strong scaling (that is the wall-clock time speedup as a function of the number of processors used for a system of fixed size) due to the very high degree of parallelization of the entire code. This comes together with a reduced required memory per core. These peculiarities made possible the computation on large systems (containing several hundreds or thousands of atoms per cell), with little or no point-symmetry particularly, when a coarse reciprocal space sampling is possible. The calculations were performed at the SuperMUC phase-1 (LRZ, Germany) [77] HPC IBM iDataPlex machine powered by 16 Intel cores per node running at 2.7 GHz, with 2GB/core. A typical calculation was run on 1024-2048 cores.

TZVP basis sets have been employed for Mg atoms [78] and Cl atoms [79], except for the outermost *sp* and *d* shells of Cl and Mg [66], where the exponents have been adjusted at the values reported in a previous paper by some of us in view of energy minimisation for the unit cell of cubic packed $MgCl_2$ α-form. Similarly, for Ti atoms [80] the basis was derived according to reference [66].

For each cell a Γ-centred Pack-Monkhorst grid has been used for sampling the reciprocal space [81]. These consisted of at least 16 **k**-points in the First Brillouin Zone, depending on the examined system.

The DFT exchange-correlation contribution and its gradient are evaluated by numerical integration over the unit cell volume [82, 83], where the generation of the integration grid points is based on an atomic partition method, originally developed by

Becke for molecules [84], and further extended to periodic systems. Within this scheme, the unit cell is partitioned into atomic volumes centered on the nuclei, where each point has an associated weight. Radial and angular points for the integration grid are generated by Gauss-Legendre quadrature and Lebedev two-dimensional distributions, respectively. The choice of a suitable grid is crucial for both numerical accuracy and the optimisation of computational resources. In this work, a default pruned grid with 99 radial and 1454 angular points has been used. The threshold in energy variation of SCF cycles was set equal to 10^{-8} Hartree for geometry optimization and equal to 10^{-13} for frequency calculations. Full relaxation of internal coordinates and cell parameters has been carried out.

3.2.2 Vibrational frequencies and thermodynamic analysis

Harmonic phonon frequencies ω_p at the Γ point (i.e. the center of the first Brillouin zone in the reciprocal space) were obtained from the diagonalization of the mass-weighted Hessian matrix of the second energy derivatives with respect to atomic displacement u [85-87]:

$$W^{\Gamma}_{a_i,b_j} = \frac{H^0_{ai,bj}}{\sqrt{M_a M_b}} \quad with \quad H^0_{a_i,b_j} = \left(\frac{\partial^2 E}{\partial u^0_{a_i} \partial u^0_{b_j}} \right),$$

where atoms a and b (with atomic mass M_a and M_b) in the reference cell, 0, are displayed along the i-th and j-th Cartesian directions, respectively. The second derivatives of the energy were computed as numerical derivative of the analytic nuclear gradients.

From computed harmonic vibrational frequencies, a standard statistical thermodynamics approach was adopted to estimate zero point energy and thermal correction to enthalpy and entropy contribution to get the Gibbs free energy of the investigated systems. This was then used to evaluate (i) the relative stability of the β-phase and disordered δ models with respect to α-MgCl$_2$, and (ii) the crystal morphology of MgCl$_2$ nanocrystals through surface formation Gibbs free energies.

3.2.3 Simulation of the IR spectra

Integrated intensities for IR absorption I$_p$ are computed for each mode *p* by using a computational scheme [88] based on the Berry Phase [89]. The derivatives of the dipole moment with respect to the Cartesian coordinates of atoms in the unit cell are evaluated numerically, through a scheme similar to that used for the numerical derivative of the nuclear gradients for obtaining the Hessian matrix. The IR spectrum is then simulated by adopting a pseudo-Voigt functional form consisting of Gaussian curves with full width at half maximum of 20 cm^{-1}.

4. RESULTS AND DISCUSSION

4.1 Vibrational dynamics of $MgCl_2$

4.1.1 Experimental Far-IR spectra

Figure 2A shows the Far-IR spectra of the three naked $MgCl_2$ samples. The spectrum of $MgCl_2$ A is similar to those reported in a few pioneering spectroscopic studies [20, 90, 91], although much more resolved. It is characterized by an intense and sharp absorption band at 243 cm^{-1}, with a shoulder at ca. 295 cm^{-1} and two weaker bands at ca. 370 and 410 cm^{-1}. Upon ball-milling, the Far-IR spectra greatly change in terms of relative intensity of these bands. In particular, the band at 243 cm^{-1} drastically decreases in intensity relative to the shoulder at 295 cm^{-1}, and the band at 370 cm^{-1} becomes more intense. Absorption bands in this spectral region have been generically attributed to $v(Mg-Cl)$ vibrations of bulk $MgCl_2$, but no efforts of more precise assignment can be found in the literature [20]. For this reason, we underwent a detailed computational study of the lattice vibrations for several models of $MgCl_2$, focusing the attention on the role of disorder and surface effects (vide infra).

The Far-IR spectrum of ZNC (Figure 2B) differs from those of the naked $MgCl_2$ samples in that it is less intense in the 300 - 200 cm^{-1} region, and it shows a pronounced band at ca. 435 cm^{-1}. It is worth noticing that ZNC contains also $TiCl_4$ and DBP, which can contribute to the experimental spectrum on their own, although they are present in relatively low weight percentage. The Far-IR spectrum of pure DBP (Figure S1) shows indeed a series of absorption bands in the 550 - 200 cm^{-1} region. However, by roughly normalizing its intensity to the amount of DBP present in ZNC, the contribution of DBP to the Far-IR spectrum of ZNC is negligible. In contrast, the band at ca. 435 cm^{-1} is assigned to vibrational modes involving Ti atoms. A band at a similar position was previously reported for a $MgCl_2/TiCl_4$ co-milled sample and assigned to $v(Ti-Cl)$ of Ti species in an octahedral geometry [20]. We agree with this assignment, also on the basis of the observation that this band (and not all the others) is partially consumed after reaction of ZNC with triethylaluminium (TEAl) at room temperature, as expected if a fraction of the Ti-Cl bonds are either alkylated or converted into coordination vacancies for the olefins insertion. To the best of our knowledge, this is the first Far-IR spectrum of a ZN catalyst activated by Al-alkyl.
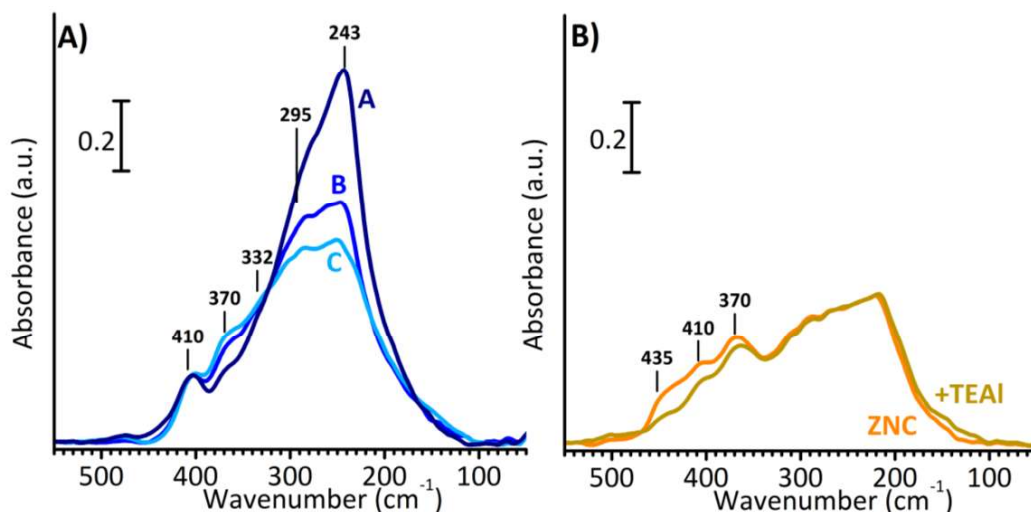
Figure 2. Experimental Far-IR spectra of MgCl$_2$ A, B and C (part A) and of ZNC before and after interaction with TEAl (part B).

4.1.2 Simulated IR spectra for bulk MgCl$_2$ (ordered and disordered models)

Before discussing the simulated IR spectra, let us comment on the relative stability of the disordered δ models (reported in Figure 1) with respect to the ordered phases. To this aim, we carried out an accurate vibrational analysis on the three δ_1, δ_2 and δ_3 disordered models to estimate the thermodynamics of the process of disordering the stable α form. The electron energy (ΔE), the enthalpy (ΔH), the entropy (ΔS), and the Gibbs free energy (ΔG) evaluated at 298 K, as reported in Table 1. Overall, disordering the α-phase is an almost spontaneous process. Indeed, the difference in enthalpy and Gibbs free energy between α and δ forms are very small, even though they fall inside the range of uncertainty of the theoretical approach. Therefore, it turns out that disordering due to stacking faults and/or rotational faults could be rather frequent in the examined compounds and could influence the vibrational spectrum.

Table 1. Total electron energy (ΔE), enthalpy (ΔH), entropy (ΔS), and Gibbs free energy (ΔG, at 298 K) for disordered δ_n models with respect to the ordered α-polymorph of MgCl$_2$ (E$_o$(α)= -1120.568362401 au cell^{-1}).

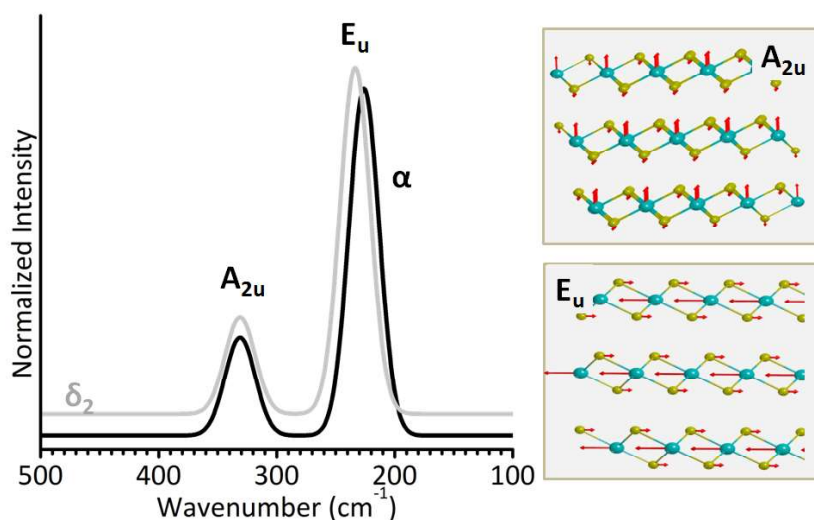| δ$_n$ model	ΔE (kJ/mol)	ΔH (kJ/mol)	$-T\Delta S$ (kJ/mol)	ΔG (kJ/mol)
δ_1	−0.070	2.00	−5.42	−3.42
δ_2	−0.050	1.90	−4.97	−3.08
δ_3	0.002	0.230	−0.043	0.186

Figure 3. Simulated Far-IR spectrum of the ordered α-MgCl$_2$ phase and of one of the three disordered models, together with a graphical representation of the two IR-active vibrational modes.

Figure 3 shows the simulated Far-IR spectrum of the ordered α-phase and of one of the three disordered models. Very similar spectra were obtained for the other δ phases and are not shown in Figure 3. Both spectra are characterized by two IR-active vibrational modes around 230 and 330 cm^{-1}, which are respectively assigned to the "intra-layer" displacement of the Mg^{2+} ions along a specific direction of the *ab* plane (E$_u$ symmetry) and to the "inter-layer" displacement of the Mg^{2+} ions parallel to the *c* axis (A$_{2u}$ symmetry). It is evident that these two modes cannot match the experimental spectra, even that of the pristine MgCl$_2$ A sample. The situation does not significantly change even by introducing different elements of disorder within the crystal structure. Indeed, whichever is the type of disorder, the E$_u$ mode is only slightly blue-shifted of a few cm^{-1}, while the other mode does not change. This outcome can be rationalised by recalling that MgCl$_2$ is a layered material with Cl-Mg-Cl layers piled up and kept together by weak dispersive interactions. Hence, the predicted results show that Far-IR spectroscopy is expected to not be greatly sensitive to the stacking/rotational disorder of MgCl$_2$, as instead X-ray diffraction has proven to be [17, 46, 92, 93].

4.1.3 MgCl$_2$ morphology and simulation of the surfaces IR spectra

To better support the interpretation of experimental Far-IR spectra, we then extended the investigation to the vibrational properties of different MgCl$_2$ surfaces, namely (001), (012),

(104), (015), (107) and (110). According to previous works by some of us [30, 56] and others [94, 95], apart from the fully saturated basal (001), the most stable surfaces belong to the families (107) and (104) (exposing weakly acidic Mg^{2+} cations) and (012), (015) and (110) (exposing strongly acidic Mg^{2+} cations). Here, the corresponding slab models were considered (fully relaxed structures are shown in Figure S2) and the surface formation energy E_s was evaluated. Then, a complete vibrational analysis was performed to include the zero-point energy, thermal corrections to enthalpy and entropic contributions, and evaluate the surface formation Gibbs free energies (G_s). For each surface, the E_s and G_s values are reported in Table 2, both of them normalized to the surface area. As already demonstrated [95], when looking to the E_s values, the surfaces exposing 5-coordinated weakly acidic Mg^{2+} cations represent the lowest energy non-trivial cuts. However, the inclusion of the entropic term changes the order of stability of the different surfaces [56], playing a decisive role when a thermodynamic approach is adopted to determine the shape of $MgCl_2$ nanocrystals.

Table 2. Inter-planar spacing d_{hkl}, Mg^{2+} coordination number, surface energy E_s, surface enthalpy H_s, surface entropy $-TS_s$, and Gibbs free energy of formation G_s for different (hkl) surfaces, number of faces predicted with the associated percentage extension in the Wulff's plot obtained using E_s and G_s, respectively.

Surface	d_{hkl} (Å)	Mg C.N.	E_s (J/m²)	H_s (J/m²)	$-TS_s$ (J/m²)	G_s (J/m²)	E_s		G_s	
							n° faces	Area (%)	n° faces	Area (%)
(001)	5.739	6	0.094	0.311	-0.261	0.050	2	52.18	2	63.54
(012)	3.001	5	0.319	0.439	-0.218	0.222	6	16.21	6	20.15
(104)	2.569	5	0.272	0.349	-0.134	0.215	6	23.76	6	7.68
(015)	2.345	5	0.281	0.396	-0.209	0.188	6	3.56	6	7.19
(107)	1.951	5	0.235	0.318	-0.135	0.183	6	3.67	0	0
(110)	1.849	4	0.396	0.654	-0.390	0.264	0	0	6	1.44

Starting from this analysis, two Wulff's polyhedra were built: the former on the basis of the energy of surface formation (E_s), which identifies a 0 K thermodynamic morphology, and the second on the basis of the Gibbs free energy (G_s), representing a model for a stable thermodynamic morphology at 298 K. Although generally E_s is a good approximation for the shape of small crystals, in a few cases free energy G_s and surface energy E_s provide different stability orders and morphologies. Indeed, Figure 4A shows the Wulff's polyhedron based on the G_s values, in comparison to that based on E_s, which is comparable to those reported in

literature [95]. It is evident that, by considering G_s rather than E_s values, the relative contribution of the surfaces exposing strongly Lewis acidic Mg^{2+} cations increases to the expenses of those exposing weakly acidic Mg^{2+} ions. In particular, the family of (107) surfaces disappears, while the (110) one appears. This is the first time that the presence of (110) surfaces emerge in a Wulff's construction of the thermodynamic morphology of $MgCl_2$. This is a remarkable result because recent quantum-mechanical investigations identified (110) faces as the catalytically active surfaces in supported ZN catalysts [66, 96-98]. Interestingly, although they account only for the 1.4% of the total surface, the existence of several edges due to the combination of adjacent faces [40, 99], such as the (110)/(104), (110)/(012) and (110)/(015) are of potential interest for catalysis. In particular, the former (110)/(104) edge has been recently considered as a privileged site for strong $TiCl_4$ adsorption to generate a stereo-selective active site [41, 67].
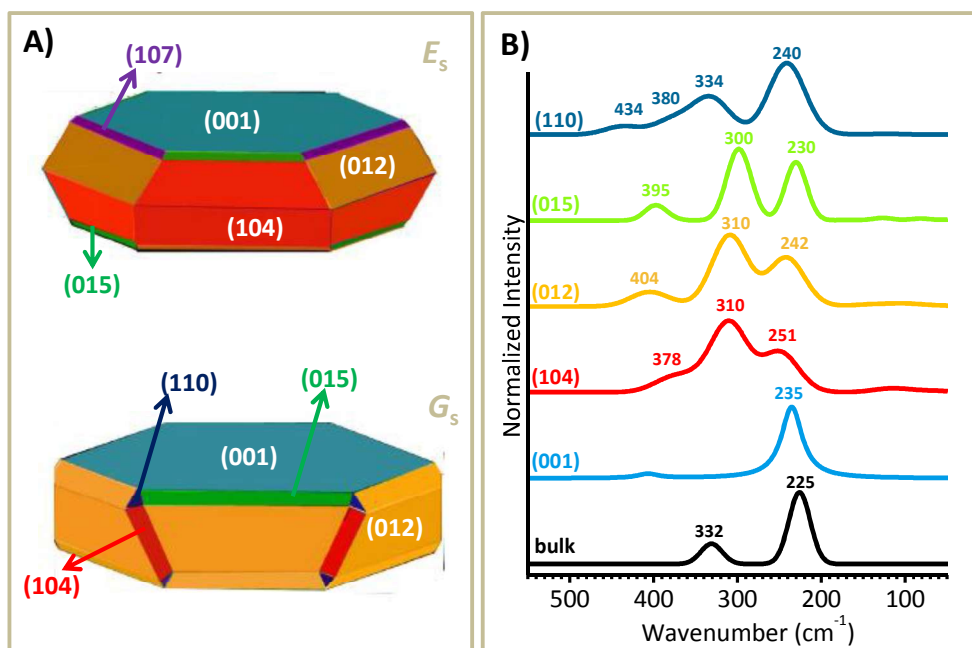

Figure 4. Part A) Wulff's polyhedra of α-$MgCl_2$ built on the basis of E_s and G_s values determined at B3LYPD2 (B3LYPD*)/TZVP level of computation. Part B) Simulated Far-IR spectra for α-$MgCl_2$ bulk and for slab models representative of (001), (104), (012), (015) and (110) surfaces. The spectra are vertically translated for clarity.

For the surfaces occurring in the G_s-based Wulff plot, a simulation of the IR spectra was carried out, as reported in Figure 4B. For all the slab models, the IR spectra are more complex than that of bulk $MgCl_2$ because of appearance of new bands, mostly related to normal modes involving surface atoms. This vibrational analysis suggests that the

experimental Far-IR spectra shown in Figure 2 contain relevant information on the exposed MgCl$_2$ surfaces and on their extension, as follows.

1) The intense and sharp band at 243 cm^{-1}, which dominates the spectrum of MgCl$_2$ A, is mainly due to the vibrational modes of the basal (001) surfaces. Upon increasing the ball-milling time, the relative extension of this surface decreases in favor of the others, indicating a change of the particle morphology, and not only a decrease in size.

2) The absorption bands at higher wavenumbers (at ca. 370 and 410 cm^{-1}) are well described by the simulated spectra of the (012), (015) and (110) surfaces. The relative contribution of these bands to the overall spectrum increases along the MgCl$_2$ A − MgCl$_2$ C series, indicating that the relative contribution of these surfaces to the overall morphology increases at long ball-milling times, in agreement with Area (%) for G_s as reported in Table 2.

3) The identification of the (104) surface is less straightforward, although it is certainly present and seems to mainly contribute to the shoulder at 295 cm^{-1}. Its relative contribution rather decreases along the MgCl$_2$ A − MgCl$_2$ C series, similar to what is observed for the basal surfaces.

4) Finally, as far as the experimental spectrum of ZNC is concerned, it lacks in intensity around 300 cm^{-1}. Among all the simulated spectra, the only one presenting a gap in that spectral region is that of the (110) surfaces. Hence, we can suggest that the relative contribution of the (110) surfaces to the overall MgCl$_2$ morphology is greater for ZNC than for the ball milled samples.

4.2 Probing surface properties of MgCl$_2$ by CO adsorption at 100 K

Finally, the accessibility of the exposed surfaces on the three ball-milled MgCl$_2$ samples and on the ZNC was probed by CO adsorption. Figure 5 shows the FT-IR spectra of CO adsorbed at 100 K, as a function of the CO coverage. It was demonstrated that this technique efficiently reveals the type and amount of exposed Mg^{2+} sites, which in turn are correlated with the extension of specific lateral surfaces [56]. The sequences of spectra are normalized to the optical thickness of the pellets, so that the absolute intensity is directly proportional to the number of adsorption sites. It is important to notice that they are shown on a different vertical scale, in order to better visualize the spectral details.
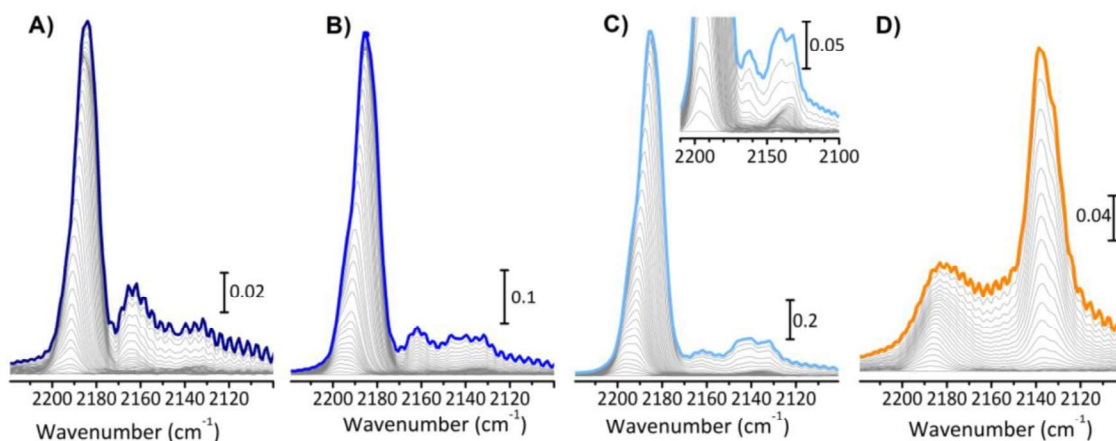
Figure 5. FT-IR spectra in the ν(CO) region of CO adsorption at 100 K on $MgCl_2$ A (part A), $MgCl_2$ B (part B), $MgCl_2$ C (part C) and ZNC (part D), as a function of CO coverage (θ_{max} in bold). The spectra are shown after subtraction of the respective baselines. The inset in part C shows a magnification of the spectra in the lower range of absorbance.

Starting the discussion from the ball-milled samples, it is evident that the absolute intensity (i.e., the amount of accessible surface sites) gradually increases across the series $MgCl_2$ A - $MgCl_2$ C, in fair agreement with the values of specific surface areas obtained by volumetric measurements. This is well evident in Figure S3, where all the four sequences of FT-IR spectra are reported in the same vertical scale. The three spectra at the maximum CO coverage (θ_{max}) are largely dominated by an absorption band at 2184 cm^{-1}, that upward shifts upon decreasing θ. This band was previously assigned to CO in interaction with strongly acidic Mg^{2+} sites [30, 56, 57, 100], which are either tetra-coordinated Mg^{2+} ions at the (110) surfaces, or penta-coordinated Mg^{2+} ions at the (012) and (015) surfaces, whereby the adsorbed CO feels the influence of a chlorine ligand from the neighboring layers as recently shown by some of us [56]. The absolute predominance of this band in the FT-IR spectra of CO adsorbed on ball-milled $MgCl_2$ samples is in good agreement with the morphological analysis discussed above.

Additional weaker bands are observed at 2197, 2162 and 2138 cm^{-1}. The band at 2162 cm^{-1} is assigned to CO coordinated to the penta-coordinated weakly acidic Mg^{2+} cations [30, 56, 57, 100]. The relative intensity of this band decreases across the $MgCl_2$ A – $MgCl_2$ C series. Hence, the longer the milling time, the more the amount of strongly acidic Mg^{2+} sites with respect to the weakly acidic Mg^{2+} sites. As far as the weak band at 2197 cm^{-1} is concerned, it is the most resistant to degassing and does not shift upon decreasing θ. Both

observations allow ascribing this band to CO in interaction with more strongly polarizing Mg^{2+} cations, which are likely low-coordinated Mg^{2+} defects. It is worth noticing that these sites were not observed on $MgCl_2$ samples obtained from the decomposition of alcoholate precursors [30, 56], because in those cases they were still in interaction with residual alcoholate moieties [32], while a similar $\nu(CO)$ band was observed for CO adsorbed on a $MgCl_2$ obtained by reacting Mg powder with butyl chloride [57]. Finally, the band at 2138 cm^{-1} is attributed to liquid-like physisorbed CO [101, 102]. Behind this band there is another one centered at 2133 cm^{-1} at θ_{max}, that is particularly evident for CO adsorbed on $MgCl_2$ C and upward shifts upon decreasing θ (inset in part C), and is assigned to a very small fraction of O-bonded CO, i.e. CO molecules interacting with Mg^{2+} sites through the oxygen atom [103-105].

Altogether, the experimental and theoretical vibrational analysis discussed in Section 4.1 and the FT-IR spectra of CO adsorbed at 100 K on the series of ball-milled $MgCl_2$ samples indicate that, at increasing milling times, the (001) basal surfaces are reduced in dimension in favor of lateral surfaces exposing strongly acidic Mg^{2+} cations, with the simultaneous formation of under-coordinated Mg^{2+} defects. This information complements the structural data reported in the first part of this work [46], providing unique evidences for the $MgCl_2$ particle size and degree of disorder.

As far as the FT-IR spectra of CO adsorbed at 100 K on ZNC is concerned, they are characterized by a much lower total intensity (see Figure S3D), although the $MgCl_2$ particle size (as determined by the structural analysis [46]) is much smaller. The reason is that the $MgCl_2$ nanoparticles are already mostly capped with $TiCl_x$ species, DBP molecules and their derivatives. The spectrum at θ_{max} is characterized by two main absorption bands in the $\nu(CO)$ region at 2138 and 2182 cm^{-1}. The former band, previously assigned to physisorbed CO [101, 102], is remarkably high for this kind of interaction (as pointed out by comparing the absolute intensities in Figure S3 with CO adsorption on ball-milled samples), indicating that ZNC shows some degree of porosity [36, 106]. The latter band is ascribed to CO in interaction with strongly acidic Mg^{2+} sites, and does not shift upon decreasing the CO coverage. The presence of this band in the FT-IR spectra of CO adsorbed at 100 K indicates that a few strongly acidic Mg^{2+} sites are still available for CO adsorption [30, 56, 57, 100], which was not expected, since these are also the sites preferentially occupied by $TiCl_x$ and donor species [56, 66]. On the contrary, no bands associated to CO interacting with weakly

acidic Mg^{2+} sites are observed (at ca. 2160 cm^{-1}). This might mean either that $MgCl_2$ particles do not expose surfaces terminating with weakly acidic Mg^{2+} cations or that those surfaces are present but capped by other molecules and hence no more accessible to CO.

5. CONCLUSIONS

A detailed investigation of the atomic dynamics in disordered and nanosized δ-$MgCl_2$ in heterogeneous Ziegler-Natta (ZN) catalysts was performed, by coupling together Far-IR spectroscopy on a series of mechanically and chemically activated $MgCl_2$ samples, and DFT calculations on both ordered and disordered models and related surfaces. These results, complemented by FT-IR spectroscopy of CO adsorbed at 100 K, gave a comprehensive picture of the morphology and surface properties of δ-$MgCl_2$ that, coupled with the structural analysis reported in the first part of this work [46], represents the most accurate investigation of δ-$MgCl_2$ in ZN catalysts ever done.

More in details, we found that the mechanical ball-milling of naked $MgCl_2$ not only promotes an increase in the total surface area, but also changes the relative extension of the surfaces, favoring the formation of the lateral surfaces exposing strongly acidic Mg^{2+} sites (i.e., the (110), (012) and (015) ones) at the expenses of the basal (001) one. Moreover, theoretical calculation predicted the existence of several possible edges involving the (110) surface. Such edges are remarkably relevant because in some recent theoretical models they were advocated as the privileged place for stereo-selective active sites [41].

On the other hand, the chemical activation of $MgCl_2$ by direct conversion of a Mg ethoxide precursor into the industrial ZN pre-catalyst leads to a much more complex situation, where most of the $MgCl_2$ surface is already occupied by the $TiCl_x$ species and the electron donors. While the structural analysis demonstrated that the stacking of the Cl-Mg-Cl layers is completely random and that the dimension of the particles is one order of magnitude smaller than what can be achieved by mechanical activation [46], the results shown in this work indicate that the relative contribution of the (110) surface to the overall $MgCl_2$ morphology is even greater than for the ball-milled samples. Moreover, FT-IR spectroscopy of CO adsorbed at 100 K revealed a significant increase in the porosity, which is a well-known parameter to be considered in catalysis for regulating the diffusion of the reagents and controlling the shape of the produced polymer.

AUTHOR INFORMATION

Corresponding Authors

*E-mail: alessandro.piovano@unito.it, maddalena.damore@unito.it

Author Contribution

A.P. performed the experiments and designed the experimental set-ups. M.D'A. developed the theoretical strategy and supervised all the theoretical work. P.C.B. performed part of the computational work, under the guidance of M.D'A.. T.W. prepared samples. A.P. and M.D'A. wrote the manuscript, that was refined by E.G.. T.W., G.T., A.T., C.P., M.T., B.C., S.B. and T.T. made analytical works and important suggestions in the framework of this collaboration. E.G. conceived the concept and supervised the entire research.

Notes

The authors declare no competing financial interest.

REFERENCES

[1]   A.T. Bell, Science 299 (2003) 1688-1691.
[2]   C.R. Henry, Prog. Surf. Sci. 80 (2005) 92-116.
[3]   P. Galli, and G. Vecellio, Prog. Polym. Sci. 26 (2001) 1287-1336.
[4]   V. Busico, R. Cipullo, A. Mingione, and L. Rongo, Ind. Eng. Chem. Res. 55 (2016) 2686-2695.
[5]   E. Albizzati, U. Giannini, G. Collina, L. Noristi, and L. Resconi, in: E.P.J. Moore, (Ed.), Polypropylene Handbook, Hanser-Gardner Publications, Cincinnati (Ohio, USA).
[6]   V. Busico, in: W. Kaminsky, (Ed.), Polyolefins: 50 years after Ziegler and Natta I, Springer, Berlin. 37-57.
[7]   V. Busico, P. Corradini, L. De Martino, A. Proto, V. Savino, and E. Albizzati, Makromol. Chem. 186 (1985) 1279-1288.
[8]   E. Iiskola, A. Pelkonen, H.J. Kakkonen, J. Pursiainen, and T.A. Pakkanen, Makromol. Chem., Rapid Commun. 14 (1993) 133-137.
[9]   B. Liu, T. Nitta, H. Nakatani, and M. Terano, Macromol. Chem. Phys. 203 (2002) 2412-2421.
[10]   P. Corradini, G. Guerra, and L. Cavallo, Acc. Chem. Res. 37 (2004) 231-241.
[11]   V. Busico, R. Cipullo, R. Pellecchia, S. Ronca, G. Roviello, and G. Talarico, Proc. Natl. Acad. Sci. 103 (2006) 15321-15326.
[12]   A. Correa, F. Piemontesi, G. Morini, and L. Cavallo, Macromol. 40 (2007) 9181-9189.
[13]   L. Wu, D.T. Lynch, and S.E. Wanke, Macromolecules 32 (1999) 7990-7998.
[14]   R. Huang, D. Liu, S. Wang, and B. Mao, Macromol. Chem. Phys. 205 (2004) 966-972.
[15]   M. Hassan Nejad, P. Ferrari, G. Pennini, and G. Cecchin, J. Appl. Polym. Sci. 108 (2008) 3388-3402.
[16]   F. Delogu, G. Mulas, L. Schiffini, and G. Cocco, Mater. Sci. Eng., A 382 (2004) 280-287.
[17]   P. Galli, P.C. Barbé, G. Guidetti, R. Zannetti, A. Marigo, M. Bergozza, and A. Fichera, Eur. Polym. Chem. 19 (1983) 19-24.
[18]   L. Noristi, P.C. Barbè, and G. Baruzzi, Makromol. Chem. 192 (1991) 1115-1127.
[19]   K. Soga, M. Ohgizawa, and T. Shiono, Makromol. Chem. 194 (1993) 2173-2181.
[20]   L. Brambilla, G. Zerbi, S. Nascetti, F. Piemontesi, and G. Morini, Macromol. Symp. 213 (2004) 287-301.
[21]   L. Brambilla, G. Zerbi, F. Piemontesi, S. Nascetti, and G. Morini, J. Mol. Catal. A-Chem. 263 (2007) 103-111.
[22]   J.S. Chung, I.K. Song, W.Y. Lee, and H.M. Park, Macromol. Chem. Phys. 196 (1995) 1205-1210.
[23]   J.H. Choi, J.S. Chung, H.W. Shin, I.K. Song, and W.Y. Lee, Eur. Polym. J. 32 (1996) 405-410.
[24]   A. Parada, T. Rajmankina, and J. Chirinos, Polym. Bull. 43 (1999) 231-238.
[25]   P. Piyavit, and P. Piyasan, Eng. J. 13 (2009) 57-64.
[26]   E. Puhakka, T.T. Pakkanen, and T.A. Pakkanen, J. Phys. Chem. A 101 (1997) 6063-6068.
[27]   A. Andoni, J.C. Chadwick, H.J.W. Niemantsverdriet, and P.C. Thune, Macromol. Rapid Commun. 28 (2007) 1466-1471.
[28]   A. Andoni, J.C. Chadwick, H.J.W. Niemantsverdriet, and P.C. Thune, J. Catal. 257 (2008) 81-86.
[29]   K.S. Thushara, R. Mathew, T.G. Ajithkumar, P.R. Rajamohanan, S. Bhaduri, and C.S. Gopinath, J. Phys. Chem. Lett. 113 (2009) 8556-8559.
[30]   K.S. Thushara, M. D'Amore, A. Piovano, S. Bordiga, and E. Groppo, ChemCatChem 9 (2017) 1782–1787.
[31]   V.H. Nissinen, I.O. Koshevoy, and T.T. Pakkanen, Dalton Trans. 46 (2017) 4452-4460.
[32]   A. Piovano, P. Pletcher, M.E.Z. Velthoen, S. Zanoni, S.-H. Chung, K. Bossers, M.K. Jongkind, G. Fiore, E. Groppo, and B.M. Weckhuysen, ChemPhysChem 19 (2018) 2662-2671.
[33]   D.N. Taveira Magalhães, O. Do Coutto Filho, and F.M.B. Coutinho, Eur. Polym. J. 27 (1991) 1093-1096.
[34]   D.H. Lee, Y.T. Jeong, and K. Soga, Ind. Eng. Chem. Res. 31 (1992) 2642-2647.

[35] A. Dashti, A. Ramazani Sa, Y. Hiraoka, S.Y. Kim, T. Taniike, and M. Terano, Polym. Int. 58 (2009) 40-45.

[36] T. Funako, P. Chammingkwan, T. Taniike, and M. Terano, Macromol. React. Eng. 9 (2015) 325-332.

[37] A. Klaue, M. Kruck, N. Friederichs, F. Bertola, H. Wu, and M. Morbidelli, Ind. Eng. Chem. Res. 58 (2019) 886-896.

[38] V. Nissinen, S. Pirinen, and T.T. Pakkanen, J. Mol. Catal. A: Chem. 413 (2016) 94-99.

[39] Y. Hiraoka, S.Y. Kim, A. Dashti, T. Taniike, and M. Terano, Macromol. React. Eng. 4 (2010) 510-515.

[40] A. Correa, R. Credendino, J.T.M. Pater, G. Morini, and L. Cavallo, Macromolecules 45 (2012) 3695-3701.

[41] R. Credendino, D. Liguori, Z. Fan, G. Morini, and L. Cavallo, ACS Catal. 5 (2015) 5431-5435.

[42] G. Morini, E. Albizzati, G. Balbontin, I. Mingozzi, M.C. Sacchi, F. Forlini, and I. Tritto, Macromolecules 29 (1996) 5770–5776.

[43] M.A. Ferrero, E. Koffi, R. Sommer, and W.C. Conner, J. Polym. Sci., Part A: Polym. Chem. 30 (1992) 2131-2141.

[44] J.A. Debling, and W.H. Ray, J. Appl. Polym. Sci. 81 (2001) 3085-3106.

[45] Z.Y. Ye, L. Wang, L.F. Feng, X.P. Gu, H.H. Chen, P.Y. Zhang, J. Pan, S. Jiang, and L.X. Feng, J. Polym. Sci., Part A: Polym. Chem. 40 (2002) 3112-3119.

[46] T. Wada, G. Takasao, A. Piovano, M. D'Amore, A. Thakur, P. Chammingkwan, P.C. Bruzzese, M. Terano, B. Civalleri, S. Bordiga, E. Groppo, and T. Taniike, J. Catal. submitted (2020).

[47] E. Magni, and G.A. Somorjai, App. Surf. Sci. 89 (1995) 187-195.

[48] E. Magni, and G.A. Somorjai, J. Phys. Chem. 100 (1996) 14786-14793.

[49] E. Magni, and G.A. Somorjai, Surf. Sci. 345 (1996) 1-16.

[50] E. Magni, and G.A. Somorjai, J. Phys. Chem. B 102 (1998) 8788-8795.

[51] T. Risse, J. Schmidt, H. Hamann, and H.J. Freund, Angew. Chem. Int. Ed. 41 (2002) 1518-1520.

[52] J. Schmidt, T. Risse, H. Hamann, and H.J. Freund, J. Chem. Phys. 116 (2002) 10861-10868.

[53] H.J. Freund, M. Baumer, J. Libuda, T. Risse, G. Rupprechter, and S. Shaikhutdinov, J. Catal. 216 (2003) 223-235.

[54] A. Andoni, J.C. Chadwick, S. Milani, H. Niemantsverdriet, and P.C. Thune, J. Catal. 247 (2007) 129-136.

[55] A. Andoni, J.C. Chadwick, J.W. Niemantsverdriet, and P.C. Thune, Catal. Lett. 130 (2009) 278-285.

[56] M. D'Amore, K.S. Thushara, A. Piovano, M. Causà, S. Bordiga, and E. Groppo, ACS Catal. 6 (2016) 5786–5796.

[57] V.A. Zakharov, E.A. Paukshtis, T.B. Mikenas, A.M. Volodin, E.N. Vitus, and A.G. Potapov, Macromol. Symp. 89 (1995) 55.

[58] A. Correa, N. Bahri-Laleh, and L. Cavallo, Macromol. Chem. Phys. 214 (2013) 1980-1989.

[59] P. Corradini, V. Barone, R. Fusco, and G. Guerra, Eur. Polym. J. 15 (1979) 1133-1141.

[60] M. Boero, M. Parrinello, and K. Terakura, J. Am. Chem. Soc. 120 (1998) 2746-2752.

[61] M. Boero, M. Parrinello, S. Hüffer, and H. Weiss, J. Am. Chem. Soc. 122 (2000) 501-509.

[62] M. Boero, M. Parrinello, H. Weiss, and S. Huffer, J. Phys. Chem. A 105 (2001) 5096-5105.

[63] G. Monaco, M. Toto, G. Guerra, P. Corradini, and L. Cavallo, Macromolecules 33 (2000) 8953-8962.

[64] M. Seth, P.M. Margl, and T. Ziegler, Macromolecules 35 (2002) 7815-7829.

[65] T. Taniike, and M. Terano, Macromol. Rapid Commun. 29 (2008) 1472-1476.

[66] M. D'Amore, R. Credendino, P.H.M. Budzelaar, M. Causá, and V. Busico, J. Catal. 286 (2012) 103–110.

[67] E. Breuza, G. Antinucci, P.H.M. Budzelaar, V. Busico, A. Correa, and C. Ehm, Int. J. Quantum Chem. 118 (2018) e25721.

[68]   E. Breuza, G. Antinucci, P.H.M. Budzelaar, V. Busico, A. Correa, and C. Ehm, J. Phys. Chem. C 122 (2018) 9046-9053.

[69]   M.A. Bañares, Catal. Today 100 (2005) 71-77.

[70]   E. Groppo, K. Seenivasan, and C. Barzan, Catal. Sci. Technol. 3 (2013) 858-878.

[71]   R. Dovesi, B. Civalleri, C. Roetti, V.R. Saunders, and R. Orlando, in: K.B. Lipkowitz, R. Larter, and T.R. Cundari, (Eds.), Reviews in Computational Chemistry, Wiley-VCH. 1-125.

[72]   M. Terano, H. Soga, and K. Kimura, US 4,829,037 (1989).

[73]   S. Grimme, J. Comput. Chem. 27 (2006) 1787-1799.

[74]   B. Civalleri, C.M. Zicovich-Wilson, L. Valenzano, and P. Ugliengo, CrystEngComm 10 (2008) 405-410.

[75]   S. Grimme, J. Antony, S. Ehrlich, and H. Krieg, J. Chem. Phys. 132 (2010).

[76]   R. Dovesi, A. Erba, R. Orlando, C.M. Zicovich-Wilson, B. Civalleri, L. Maschio, M. Rérat, S. Casassa, J. Baima, S. Salustro, and B. Kirtman, WIREs Comput. Mol. Sci. 8 (2018) e1360.

[77]   https://www.lrz.de/services/compute/supermuc/systemdescription/. SuperMUC Petascale System.

[78]   L. Valenzano, Y. Noël, R. Orlando, C.M. Zicovich-Wilson, M. Ferrero, and R. Dovesi, Theor. Chem. Acc. 117 (2007) 991-1000.

[79]   E. Apra, M. Causa, M. Prencipe, R. Dovesi, and V.R. Saunders, J. Phys. Condens. Matter 5 (1993) 2969.

[80]   F. Corà, Mol. Phys. 103 (2005) 2483-2496.

[81]   H.J. Monkhorst, and J.D. Pack, Phys. Rev. B 13 (1976) 5188-5192.

[82]   R. Dovesi, R. Orlando, A. Erba, C.M. Zicovich-Wilson, B. Civalleri, S. Casassa, L. Maschio, M. Ferrabone, M. De La Pierre, P. D'Arco, Y. Noël, M. Causà, M. Rérat, and B. Kirtman, Int. J. Quantum Chem. 114 (2014) 1287-1317.

[83]   R. Dovesi, V.R. Saunders, C. Roetti, R. Orlando, C.M. Zicovich-Wilson, F. Pascale, B. Civalleri, K. Doll, N.M. Harrison, I.J. Bush, P. D'Arco, M. Llunell, M. Causà, and Y. Noël. 2014. Crystal14.

[84]   A.D. Becke, J. Chem. Phys. 88 (1988) 2547-2553.

[85]   F. Pascale, C.M. Zicovich-Wilson, F. López Gejo, B. Civalleri, R. Orlando, and R. Dovesi, J. Comput. Chem. Phys. 25 (2004) 888-897.

[86]   C.M. Zicovich-Wilson, F. Pascale, C. Roetti, V.R. Saunders, R. Orlando, and R. Dovesi, J. Comput. Chem. Phys. 25 (2004) 1873-1881.

[87]   C. Carteret, M. De La Pierre, M. Dossot, F. Pascale, A. Erba, and R. Dovesi, J. Chem. Phys. 138 (2013) 014201.

[88]   S. Dall'Olio, R. Dovesi, and R. Resta, Phys. Rev. B 56 (1997) 10105-10114.

[89]   R.D. King-Smith, and D. Vanderbilt, Phys. Rev. B 49 (1994) 5828-5844.

[90]   V. Di Noto, R. Zannetti, M. Vivani, C. Marega, A. Marigo, and S. Bresadola, Makromol. Chem. 193 (1992) 1653-1663.

[91]   V. Di Noto, and S. Bresadola, Macromol. Chem. Phys. 197 (1996) 3827-3835.

[92]   A. Martorana, R. Zannetti, A. Marigo, D. Ajo, and V. Malta, Comput. Phys. Commun. 27 (1982) 49-55.

[93]   G. Giunchi, and G. Allegra, J. Appl. Cryst. 17 (1984) 172-178.

[94]   V. Busico, M. Causà, R. Cipullo, R. Credendino, F. Cutillo, N. Friederichs, R. Lamanna, A. Segre, and V. Van Axel Castelli, J. Phys. Chem. C 112 (2008) 1081-1089.

[95]   R. Credendino, V. Busico, M. Causà, V. Barone, P.H.M. Budzelaar, and C. Zicovich-Wilson, Phys. Chem. Chem. Phys. 11 (2009) 6525-6532.

[96]   E. Puhakka, T.T. Pakkanen, and T.A. Pakkanen, Surf. Sci. 334 (1995) 289-294.

[97]   T. Taniike, and M. Terano, J. Catal. 293 (2012) 39-50.

[98]   R.H. Cheng, J. Luo, Z. Liu, J.W. Sun, W.H. Huang, M.G. Zhang, J.J. Yi, and B.P. Liu, Chinese J. Polym. Sci. 31 (2013) 591-600.

[99]   A. Bazhenov, M. Linnolahti, T.A. Pakkanen, P. Denifl, and T. Leinonen, J. Phys. Chem. C 118 (2014) 4791-4796.

[100]   D.A. Trubitsyn, V.A. Zakharov, and I.I. Zakharov, J. Mol. Catal. A: Chem. 270 (2007) 164-170.

[101]   G. Ghiotti, E. Garrone, C. Morterra, and F. Boccuzzi, J. Phys. Chem. 83 (1979) 2863-2869.

[102]   A. Zecchina, and C. Otero Areán, Chem. Soc. Rev. 25 (1996) 187-197.

[103]   C. Otero Areán, M. Rodríguez Delgado, O.V. Manoilova, G. Turnes Palomino, A.A. Tsyganenko, and E. Garrone, Chem. Phys. Lett. 362 (2002) 109-113.

[104]   P.Y. Storozhev, V.S. Yanko, A.A. Tsyganenko, G. Turnes Palomino, M. Rodríguez Delgado, and C. Otero Areán, Appl. Surf. Sci. 238 (2004) 390-394.

[105]   T. Montanari, P. Kozyra, I. Salla, J. Datka, P. Salagre, and G. Busca, J. Mater. Chem. 16 (2006) 995-1000.

[106]   T. Taniike, P. Chammingkwan, V.Q. Thang, T. Funako, and M. Terano, Appl. Catal.: A Gen. 437-438 (2012) 24-27.

SUPPORTING INFORMATION

Revisiting the identity of δ-MgCl₂: Part II. Morphology and exposed surfaces studied by vibrational spectroscopies and DFT calculation.

Alessandro Piovano,*[‡,§] Maddalena D'Amore,*[‡] Toru Wada,[†,§] Paolo Cleto Bruzzese,[‡] Gentoku Takasao,[†] Ashutosh Thakur,[†] Patchanee Chammingkwan,[†,§] Minoru Terano[†,§], Bartolomeo Civalleri,[‡] Silvia Bordiga,[‡] Toshiaki Taniike,[†,§] and Elena Groppo[‡,§]

[‡] Department of Chemistry, INSTM and NIS Centre, University of Torino, Via Quarello 15, 10135 Torino, Italy

[§] Dutch Polymer Institute, P.O. Box 902, 5600 AX Eindhoven, the Netherlands

[†] Graduate School of Advanced Science and Technology, Japan Advanced Institute of Science and Technology, 1-1 Asahidai, Nomi, Ishikawa, 923-1292, Japan
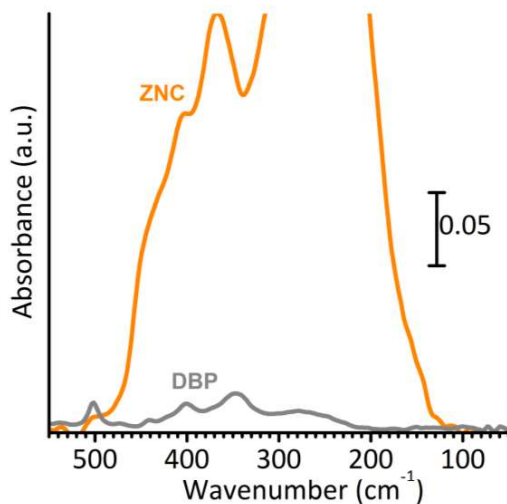
Figure S1. Far-IR spectrum of pure DBP in comparison with the spectrum of ZNC, the former rescaled in intensity for the content of DBP in ZNC sample (14.1 wt%).
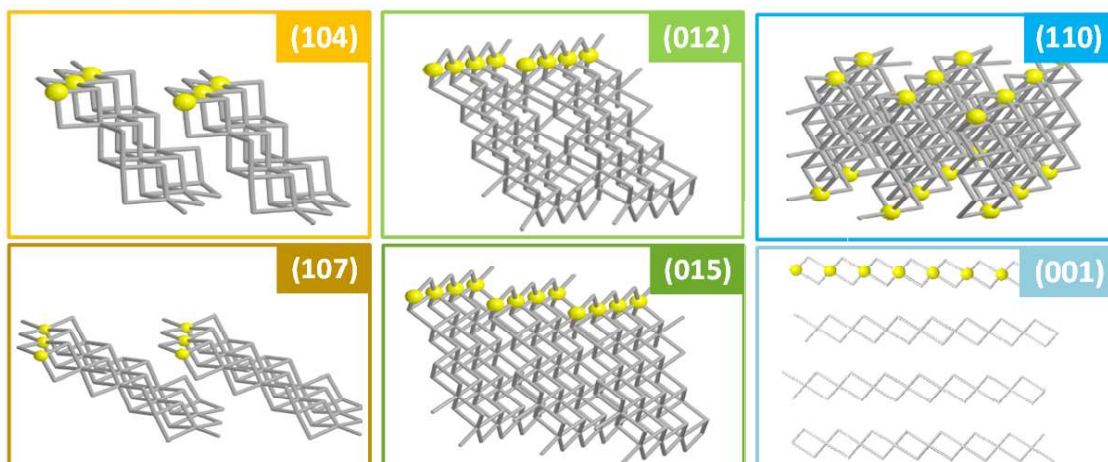
Figure S2. Slab models for the different MgCl$_2$ surfaces after relaxation. Mg^{2+} sites exposed on the surfaces are represented as yellow balls, while all the rest of the framework as grey sticks.
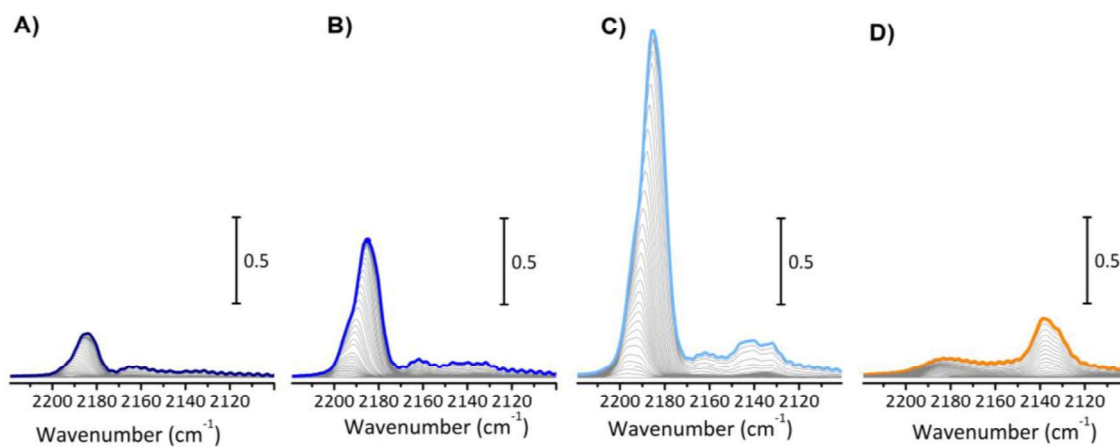

Figure S3. Same FT-IR spectra in the v(CO) region as in Figure 8, but with the fixed vertical scale (after normalizing the spectra by the optical thickness of the pellets). Briefly, CO adsorption at 100 K on MgCl$_2$ A (part A), MgCl$_2$ B (part B), MgCl$_2$ C (part C) and ZNC (part D), as a function of CO coverage (θ_{max} in bold).

GRAPHICAL ABSTRACT